






Mesoscopic axially swept oblique plane microscope for the imaging of freely moving organisms with near-isotropic resolution

SAMUEL DAVIS,¹ JON-RICHARD SOMMERNES,² SEBASTIAN HAMBURA,^{1,3} LEVIN RIEDEL,^{4,5} ALEJANDRO GIL,^{3,6} AISSAM IKMI,⁴  FLORIAN STRÖHL,²  AND ROBERT PREVEDEL^{1,4,7,8,*} 

¹Cell Biology and Biophysics Unit, European Molecular Biology Laboratory, Heidelberg, Germany

²Department of Physics and Technology, UiT The Arctic University of Norway, Tromsø, Norway

³Suricube GmbH, Heidelberg, Germany

⁴Developmental Biology Unit, European Molecular Biology Laboratory, Heidelberg, Germany

⁵Collaboration for joint PhD degree between EMBL and Heidelberg University, Faculty of Biosciences, Heidelberg, Germany

⁶Core Facilities Unit, European Molecular Biology Laboratory, Heidelberg, Germany

⁷Epigenetics and Neurobiology Unit, European Molecular Biology Laboratory, Monterotondo, Italy

⁸Molecular Medicine Partnership Unit (MMPU), European Molecular Biology Laboratory, Heidelberg, Germany

*prevedel@embl.de

Abstract: Rapid three-dimensional imaging over extended fields of view (FOVs) is crucial to the study of organism-wide systems and biological processes *in vivo*. Selective-plane illumination microscopy (SPIM) is a powerful method for high spatio-temporal resolution *in toto* imaging of such biological specimens. However, typical SPIM implementations preclude conventional sample mounting and have anisotropic imaging performance, in particular when designed for large FOVs over 1 mm diameter. Here, we introduce axial sweeping of the illumination into a non-orthogonal dual-objective oblique plane microscope (OPM) design, thereby enabling the observation of freely moving animals over millimeter-sized FOVs, at close to isotropic, sub-cellular resolution. We apply our mesoscopic axially swept OPM (MASOPM) to image the behavioral dynamics of the sea anemone *Nematostella vectensis* over $1 \times 0.7 \times 0.4$ mm at $1.7 \times 2.6 \times 3.7$ μm resolution and 0.5 Hz volume rate.

© 2024 Optica Publishing Group under the terms of the [Optica Open Access Publishing Agreement](#)

1. Introduction

Light-sheet fluorescence microscopy has enabled three-dimensional imaging of sensitive biological processes *in vivo* at high speed and for long periods, due to parallelized detection and low illumination intensities, respectively [1]. Despite these clear advantages, applications of SPIM to bio-imaging remain highly specialized. The major factors that limit greater use are unconventional sample mounting, and inhomogeneous and anisotropic imaging quality. The use of two orthogonal objectives, for illumination and fluorescent detection, in conventional SPIM precludes the use of standard mounting methods – such as microscopy slides and glass bottomed petri-dishes. Oblique plane microscopy (OPM) was developed to overcome this limitation, while keeping the benefits of high speed and low illumination intensities [2,3]. By illuminating and imaging a plane at an oblique angle to the focal plane of the primary objective, the need for an orthogonal illumination objective is removed and conventional sample mounting can be used.

A growing number of OPM systems have been developed to take advantage of light-sheet imaging with conventional mounting [4–8]. However, it is challenging to design an OPM system for lower magnification imaging, which is typically necessary for whole-organism studies and developmental biology research that require capturing larger FOVs to observe dynamic biological

processes comprehensively. In OPM, the imaged plane is at an oblique angle to the focal plane of the primary objective. A remote refocusing scheme is required to reimage the out of focus plane and achieve aberration free imaging [9]; an intermediate image plane is formed and reimaged by a tilted tertiary objective. The tilted alignment between the secondary and tertiary objectives leads to a reduction in fluorescent collection efficiency and imaging performance – due to partial overlap of their respective light cones. This issue deteriorates rapidly with decreasing numerical aperture (NA); not only do the light cones get smaller, but the oblique angle gets steeper – leading to complete loss for $NA < 0.5$ [10]. The collection efficiency can be improved using a diffraction grating or fiber optical faceplate in the intermediate image plane [10,11]. However, this does not address the steep illumination angle in object space. Since the system PSF is a product of illumination and detection contributions, this steep angle yields an axially elongated PSF and poor axial resolution of $>20\ \mu\text{m}$ – which is not sufficient to resolve individual cells of most model organisms which tend to be in the range of $5\text{--}15\ \mu\text{m}$. The oblique angle can be reduced using reflective optics in object space, however such solutions typically come with limitations and/or impracticalities regarding the sample mounting and require specialized micro-optics [12,13].

We previously reported an OPM system tailored for mesoscopic FOVs over 1 mm in size [14], that overcame these issues using a non-orthogonal dual-objective design inspired by Glaser et al. [15]. As in a conventional SPIM system, a second objective is used for illumination, however, at an oblique angle of only 25° with respect to the imaging objective. In this non-orthogonal dual-objective (NODO) configuration, the illumination objective lies entirely below the imaging plane and therefore avoids any steric hindrance with respect to sample mounting. While this design afforded ‘open-top’ access at mesoscopic FOVs and enabled first applications to freely moving animals, its spatial resolution was highly anisotropic at $< 1.5 \times 5.3\ \mu\text{m}$ in the lateral and axial direction, respectively, as well as non-homogenous over its (axial) FOV. This can be particularly limiting for dynamic samples such as freely moving animals since their orientation and position is ever changing and potential inhomogeneities in resolution can thus hinder quantitative and longitudinal image analysis and tracking tasks.

To overcome these limitations in mesoscopic OPMs, here we introduce axial sweeping [16–21] of the illumination light in order to substantially improve the imaging system’s axial resolution as well as rendering it near-uniform over a larger axial FOV, from 0.2 to 0.6 mm. By utilizing a higher NA illumination and sweeping the waist synchronously with the active pixels of the rolling shutter of the camera, out-of-focus illumination is rejected and a well confined light-sheet can effectively be realized over a greater axial FOV. We demonstrate this by imaging live, freely moving *Nematostella* polyps, where the extended FOV and improved axial resolution allows to capture and tolerate vertical sample motion, variable orientation of the body column, and larger peristaltic movements.

2. Methods

2.1. MASOPM principle

In OPM, the illumination and detection planes are tilted relative to the nominal focal plane of the objective. In general use, microscope objectives can only produce a diffraction limited image of their focal plane. However, if a secondary microscope is used to create a remote refocusing system with equal lateral and axial magnification, a diffraction limited image of the whole 3D sample is formed. This can then be reimaged by the tertiary objective, which is tilted and aligned to the intermediate image of the obliquely illuminated plane. It is here where the majority of light loss occurs in single-objective OPMs. The use of a second non-orthogonal illumination objective allows the light cone overlap between the secondary and tertiary objectives to be improved, without the use of gratings (Fig. 1(a) inset).

Single-objective OPMs also have a limitation on illumination numerical aperture [2]. With the NODO approach the whole illumination objective NA is available, which we can make use of

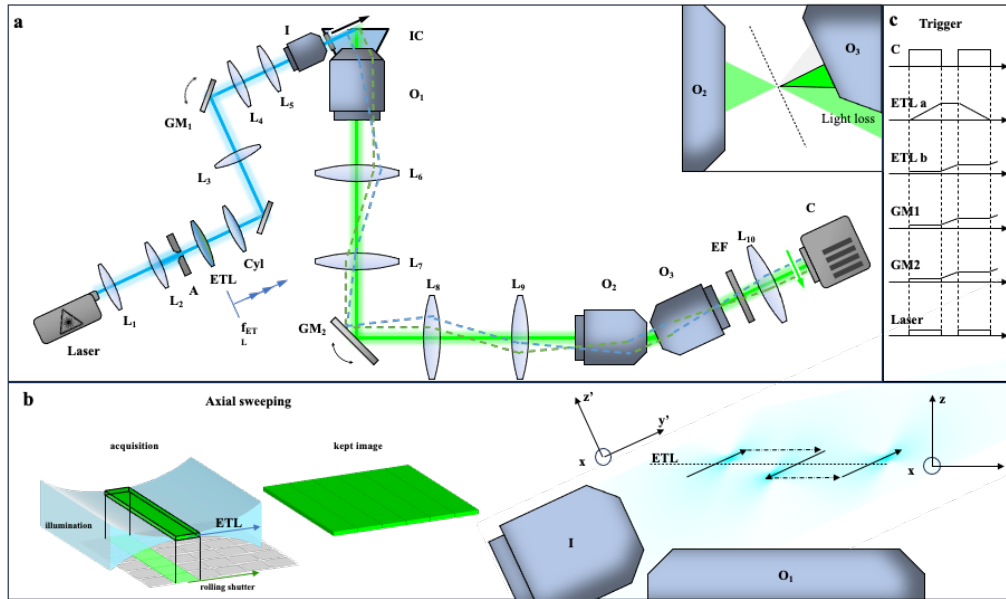


Fig. 1. Schematic of the MASOPM system. (a) Optical layout of the microscope. The illumination objective (I) launches the light-sheet into the immersion chamber (IC) through a glass window that lies perpendicular to the propagation axis of the light-sheet. The fluorescence signal is then collected by the primary objective (O_1) and the volume refocused to the intermediate image plane between the secondary objective (O_2) and tertiary objective (O_3), as shown in the inset. (b) Left: Principle of axial sweeping. While each frame is acquired, the ETL is used to scan the light-sheet focus in its propagation direction synchronously with the rolling shutter of the camera. Right: ETL adjustment. During a volumetric scan, the light-sheet must also be shifted between frames to keep the sweep centered at the focal plane of O_1 . (c) System synchronization. The ETL is driven by the sum of ETL a and ETL b functions. ETL a sweeps the light-sheet synchronously with the image sensor's rolling shutter, and ETL b keeps the sweep centered on the focal plane of the detection objective as the light sheet is scanned.

with axial sweeping. With a conventional gaussian light-sheet, there is a trade-off between how tightly the light-sheet is focused, its waist, and the length over which that focus can be maintained. For example, a 1 mm long, 488 nm light-sheet in water, would limit the waist and thus axial thickness of the light-sheet to $\sim 7.6 \mu\text{m}$. If the light-sheet is more tightly focused, the imaging quality varies across the FOV – with good axial sectioning around the waist, and decreased sectioning and thus increased background elsewhere. To achieve a tighter focus across the whole FOV, the light-sheet waist can be swept synchronously with the active pixel region of the camera [17,20], thereby only keeping a well sectioned portion of the image. By doing this over the full FOV the axial resolution becomes uncoupled from the depth-of-focus of the original high-NA light-sheet (Fig. 1(b)). Axial sweeping is conventionally performed by a moving mirror in a remote focusing space along the optical axis of the illumination objective. While this geometry is challenging to realize in a single-objective OPM system, it is straightforward in a NODO OPM configuration. Further, as the illumination NA in our mesoscopic system is small compared to high-resolution SPIM systems, it is feasible to axially move the light-sheet waist using an electrically-tunable-lens (ETL) without the additional complexity of another remote focusing space – removing the need for another objective, and the inertial barrier to speed.

2.2. Microscope design

The schematic design of our MASOPM is illustrated in Fig. 1. The microscope is designed with an ‘open-top’ geometry (Fig. 1(a)); samples can be placed on top of the imaging chamber in standard glass bottom dishes, microscope slides, or a custom designed sample holder. The sample is illuminated by a 488 nm continuous wave laser (Laser, Olympus Cell*). The beam is fiber coupled and expanded using a telescope (L1 and L2, Linos) before passing through an electrically tunable lens (ETL, Optotune EL-10-30-C-VIS-LD-MV), calibrated to be at 0 dpt at the centre of the FOV. A static light-sheet is generated using a cylindrical lens (Cyl, $f = 50$ mm, Thorlabs LJ1695RM-A), and relayed onto the sample using tube lenses (L3, L4, and L5, Plössl type-2× Thorlabs AC254-125-A) and an objective lens (I, 5X 0.14 NA air Mitutoyo M Plan Apo), which lies at an angle of 25° relative to the image plane of the primary objective (O1, 10X 0.5 NA glyc Nikon MRD71120, field-number 22, WD 5.5 mm). A galvanometric mirror (GM1, Hans scanner $\pm 22.5^\circ$), conjugate to the back focal plane of the objective, scans the light-sheet over the sample.

The sample volume is imaged to the intermediate image volume by two microscopes in series, coupled by a relay. The first is composed of O1 and L6 ($f = 200$ mm, Thorlabs TTL200MP), the relay is formed by L7 and L8 ($f = 200$ mm, Thorlabs TTL200MP), and the second microscope of L9 ($f = 150$ mm, custom) and the secondary objective (O2, 10X 0.45 NA air Nikon MRD00105). The back-focal planes of O1 and O2 are conjugated to the galvo mirror GM2 in the relay, which is used to descanned the imaged volume. The tube lenses L6 and L9 are chosen such that their focal lengths match the ratio of the refractive indices at the primary and the secondary objective so that the lateral and axial magnifications are equal. A tertiary objective (O3, 10X 0.45 NA air Nikon MRD00105) is aligned relative to the secondary objective such that its focal plane is coincident with the descanned image of the illuminated plane. The intermediate oblique image plane is then finally reimaged onto a sCMOS camera (Kinetix, Teledyne Photometrics) using a tube lens (L10, $f = 200$ mm, Thorlabs TTL200A), via an emission filter (EF, Semrock FF01-520/35-25). All devices are synchronized and controlled using a new, custom FPGA-based hardware controller (Galaxy from Suricube GmbH). This controller allows the simple generation of various synchronous traces at 1 MHz update rate, including pulses, staircase and ramp signals, which we make particular use of for the dual functionality of the ETL (Fig. 1(c)). The hardware controller is controlled using JSON text files which set the parameters important for system synchronization, and are sent by a generic MQTT client. A schematic overview of the imaging system is shown in Fig. 1(a).

2.3. Axial sweeping implementation

We utilize an ETL to control the position of the light-sheet waist in two ways. Firstly, we sweep the waist position axially, synchronously with the rolling shutter of the camera in order to improve axial resolution without sacrificing FOV (Fig. 1(b)). Secondly, because the illumination and imaging scan directions are at an oblique angle, the waist must be adjusted during a lateral (volumetric) scan to keep it at the focal plane of the detection objective (Fig. 1(b),(c)). The direction of the ETL axial-sweep and the camera’s rolling shutter is alternated frame to frame to maximise speed.

The effective width of a camera’s rolling shutter can be controlled by adjusting the readout delay between adjacent camera pixel rows, which at a minimum is 3.75 μ s for our camera (Kinetix, Teledyne Photometrics). With this delay, using a 1 ms row exposure gives an effective rolling shutter width of 267 pixels or 130 μ m at the sample. This approximately matches the depth-of-focus of the high NA illumination, shown in Fig. 2(b). The slight excess tolerance acts as a compromise between sectioning and sensitivity, and allows for some variation in the calibration of the ETL’s optical power. With these settings there is no speed cost in comparison to a non-axially swept acquisition. If a longer exposure is required for dimmer fluorescent labels,

then the delay between rows must be increased to give the same rolling shutter width, which would reduce the frame rate in comparison to a non-axially swept acquisition.

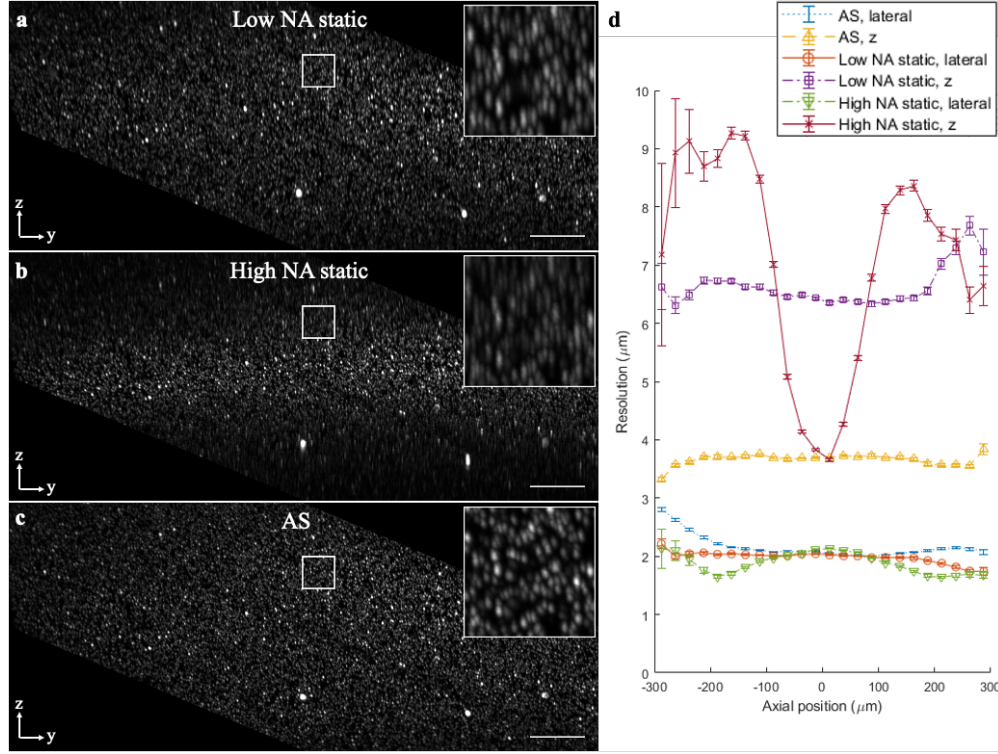


Fig. 2. Optical characterization of the MASOPM system. (a-c) Reconstructed lab space 3D image stack of beads acquired using low NA static light-sheet, high NA static, and axially swept (AS) light-sheet, respectively, over the FOV of $1.5 \times 1.1 \times 0.6 \text{ mm}^3$, projected along the x -axis (yz -plane). Inset: Zoom-in to region of interest indicated by white box. (d) FOV analysis. The resolution is plotted for different regions of the axial FOV to illustrate the spatial dependence of the resolution across the 3D FOV. Scale-bars 100 μm .

2.4. 3D volume reconstruction

In oblique plane microscopy, a 3D volume is acquired in a sheared geometry. To recover an undistorted volumetric image, the raw data and image stack must be ‘de-sheared’ into the correct rectilinear lab coordinate system. To do so, an affine transformation has to be applied to the 3D dataset [22]. This transformation is a combination of a shear to the oblique coordinate system, and a rotation into lab space:

$$M = \begin{bmatrix} 1 & 0 & 0 & 0 \\ 0 & \cos(\theta) & \sin(\theta) & 0 \\ 0 & -\sin(\theta) & \cos(\theta) & 0 \\ 0 & 0 & 0 & 1 \end{bmatrix} \begin{bmatrix} 1 & 0 & 0 & 0 \\ 0 & 1 & 1/\tan(\theta) & 0 \\ 0 & 0 & 1 & 0 \\ 0 & 0 & 0 & 1 \end{bmatrix} \quad (1)$$

The transformation was performed in Matlab. To reduce axial sampling requirements, interpolation is performed in a coordinate system aligned with the point spread function rather

than the sampling grid. The effect of this is shown in Fig. S1. Using conventional interpolation without oversampling in z' will have a significant effect on the resolution, and lead to pronounced artefacts.

3. Results

3.1. Optical characterization

The optical performance of our MASOPM system was characterized by imaging 1.1 μm diameter beads (Thermo Scientific Fluoro-Max green) suspended in 0.5% agarose. The bead phantom was imaged with an axially swept acquisition, and with two static light-sheets; one with the full illumination aperture (high NA static), and one with the numerical aperture limited to 0.02, in order to match its size to the swept case, i.e. 1 mm in length (low NA static). The FOV in x' and y' was 1.5 mm x 1.5 mm, and 800-images were acquired with a z' separation of 0.5 μm . This gave a lab space volume of 1.5 mm x 1.1 mm x 0.6 mm. The resolution was quantified by calculating the full-width at half maximum (FWHM) of the beads, using linear interpolation, across the FOV in the axial and lateral directions in the lab coordinate system. Figure 2 summarizes these findings.

Figure 2(a-c) shows the maximum intensity projection of the reconstructed 3D stack (3200 planes) in the x direction, acquired with a low NA static light-sheet, and high NA static light-sheet, and an axially swept light-sheet, respectively. The spatial dependence of the resolution across the axial FOV is shown in Fig. 2(d). The useable lateral and axial FOV for the MASOPM, high NA static, and low NA static acquisition 1.1 x 0.6 mm, 1.1 x 0.1 mm, and 1.1 x 0.6 mm, respectively. The axial FOV of our MASOPM implementation is limited by the sensor size and choice of oblique angle. The resolution within the useable FOV, for the MASOPM ($N = 15490$ beads), high NA static ($N = 3887$ beads), and low NA static ($N = 13694$ beads) acquisition in x , y , and z was found to be: $1.7 \pm 0.4 \mu\text{m}$, $2.6 \pm 0.5 \mu\text{m}$, and $3.7 \pm 0.6 \mu\text{m}$; $1.8 \pm 0.4 \mu\text{m}$, $2.4 \pm 0.3 \mu\text{m}$, and $4.3 \pm 1.1 \mu\text{m}$; $1.6 \pm 0.4 \mu\text{m}$, $2.4 \pm 0.5 \mu\text{m}$, and $6.5 \pm 1.3 \mu\text{m}$, respectively. The lateral resolution matches the performance from our previously reported system [14] – but using the entire aperture of the illumination objective gives an enhancement to axial resolution of 1.8x.

3.2. Applications to freely behaving specimens

Before demonstrating the rapid and high-resolution imaging capabilities of our MASOPM system *in vivo*, we first further characterized the system on fixed *Nematostella* primary polyps. The sea anemone *Nematostella vectensis* is particularly well-suited as a model organism due to the interdependence of its developmental and behavioral dynamics, which provides a comprehensive framework for studying the intricate relationship between organismal shape and behavior [23]. Additionally, it has a relatively simple body plan composed of two epithelial layers with a complex cellular composition, including muscles and neurons. The large 3D FOV and rapid imaging speed enables *in toto* imaging of the freely behaving polyps, at cellular resolution and without sample scanning or immobilization, which would disturb and interfere with the organism's natural muscular hydraulics and development.

The *Nematostella* polyps were imaged with a FOV in x' and y' set to 1.0 mm x 1.0 mm. 200-images were acquired with a z' separation of 3.2 μm . This gave a lab space volume of 1.0 mm x 0.7 mm x 0.4 mm. The line exposure was set to 1 ms, while a camera sensor line time of 3.75 μs yielded an effective frame exposure of 8.5 ms. After an additional galvanometer settling time of 1.6 ms the total frame time was 10.1 ms, and the total volume rate was 0.5 Hz.

One-week old *Nematostella*, expressing neuron fluorescent label (Elav > mb-eGFP) [14], were fixed for system characterization. The polyps were anesthetized in 7% MgCl_2 before fixation in 4% paraformaldehyde (PFA) (EMS, E15710) in 12 ppt artificial seawater (ASW). The fixed animals were then washed with PBS with 0.2% Triton (Sigma, T8787) (PTx 0.2%)

[23]. Figure 3(a,b) shows maximum intensity projections of the reconstructed volume acquired with a static low NA light-sheet acquisition, along z and y directions respectively. Figure 3(c,d) shows the same projections for the axially swept acquisitions. The improvement in resolution is demonstrated by line profiles, and measurements of the directional Fourier shell correlation (dFSC), shown in Fig. 3(e,f) [24]. The line profile of the axially swept projection shows several features that are not resolved using the static light-sheet. Fourier correlation methods provide a holistic measure of resolution that do not make any assumptions about the sample structure or noise distribution, and is therefore an appropriate choice for characterizing imaging performance in more complex samples. The dFSC is adapted from the sectioned Fourier shell correlation to only include Fourier components within 45° of the direction of interest [25]. Using the standard cutoff of 0.143 gives an improvement in resolution from $1.7\ \mu\text{m}$, $2.0\ \mu\text{m}$, and $4.8\ \mu\text{m}$ to $1.5\ \mu\text{m}$, $1.7\ \mu\text{m}$, and $2.2\ \mu\text{m}$, in x , y , and z respectively. The axial resolution of MASOPM is 2x higher than the non-swept case, and matches quantitatively the improvement observed on the bead phantom. The small improvements observed in lateral resolution are further explained in Fig. S3.

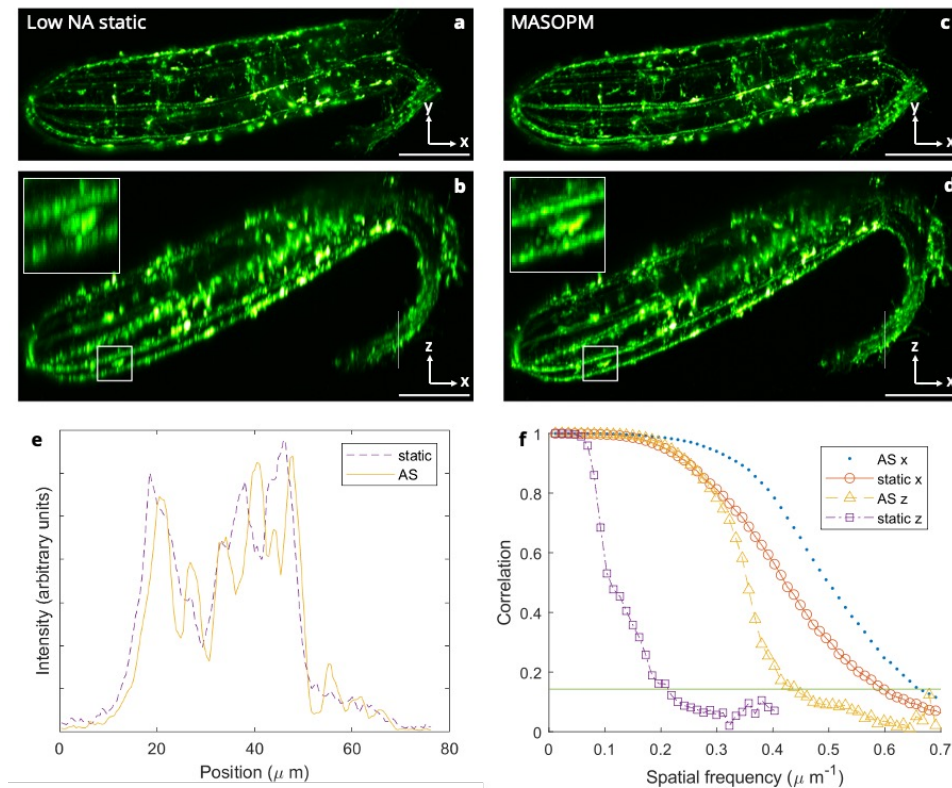


Fig. 3. Imaging of fixed *Nematostella* polyps with MASOPM. (a,b) Maximum intensity projections along the z and y directions of *Nematostella* polyp (Elav > mb-eGFP) imaged on our system with a low NA static light-sheet. (c,d) Identical polyp but using axial sweeping (MASOPM). The entire stack comprises 750 (a,c) or 1720 (b,d) planes, $0.488\ \mu\text{m}$ apart, $4.5\ \text{mW}$ excitation power. Total acquisition time for volume: 2 sec. Inset: Zoom-in to regions of interest indicated in (b,d). (e) Line profiles indicated in b and d. The axially swept (AS) acquisition resolves seven features, where only three can be seen using the static sheet. (f) Directional Fourier shell correlation (dFSC) analysis of AS and static long acquisitions. Scale-bars $100\ \mu\text{m}$.

Next, we imaged the same model organism *in vivo*. A hallmark of *Nematostella* behaviour are their whole-body peristaltic movements. We applied MASOPM using the same imaging parameters, to image *Nematostella* expressing a fluorescently tagged Myosin Heavy Chain protein (mhc::mNeonGreen) [26], labelling the muscular system (Fig. 4). With our MASOPM, we were able to capture the entire peristaltic wave, while visualizing the muscular system, with whole body movement also tolerated by the increased axial FOV. A video of maximum intensity projections is shown in [Visualization 1](#).

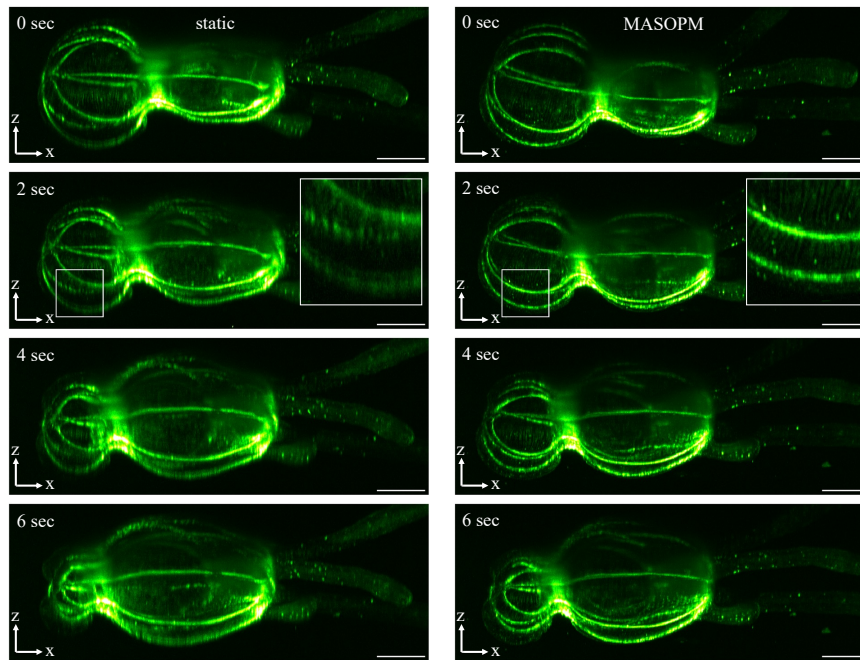


Fig. 4. Imaging of *Nematostella* polyps *in vivo* with MASOPM. Time series of *Nematostella* polyp (mhc::mNeonGreen) undergoing body contraction along oral-aboral axis. Each image is a cropped maximum intensity projection, along the y direction, of a 1.0 mm x 0.7 mm x 0.4 mm volume. The total laser power at the sample was 4.5 mW. Each volume is composed of 200 frames acquired at 100 fps, yielding a volume every 2 seconds (0.5 Hz). Also see [Visualization 1](#). Scale-bars 100 μ m.

4. Conclusion

We have introduced an OPM system for mesoscopic imaging, that combines a NODO geometry with axial sweeping of high-NA illumination using an ETL. This combination significantly improves the imaging performance in terms of contrast and resolution without increased system complexity. We demonstrated MASOPM by whole sample imaging of *Nematostella*, capturing complex behaviour such as peristaltic pumping *in vivo*.

Key to our work and particular implementation of axial sweeping is the coordination of the ETL with the camera readout – this enables an improvement to axial resolution without any additional optical complexity. The NODO geometry allows for flexibility in light-sheet design over conventional mesoscopic single-objective OPM since the oblique angle is not limited by the imaging NA. Here we have exploited this flexibility further by using the full NA of the dedicated illumination objective, which would otherwise have to be taken from the imaging NA in a single

objective light-sheet system. Compared to a very recent implementation of axial sweeping in a NODO geometry, our realization is not speed limited by a voice coil – which theoretically could acquire at 50 fps, and was demonstrated at 17 fps [21]. In our work, we achieve 100 fps while also sweeping over a significantly larger axial FOV.

MASOPM – as with other OPM methods – is more optically complex in comparison to conventional SPIM, requiring two additional objectives and challenging alignment of the remote refocusing space. However, the remote refocusing removes the need for high fidelity sample or objective scanning – instead 3D imaging is possible using only the two galvo-scanners, which can scan at effectively higher speeds. In addition, the ETL can scan the waist at the maximum speed of the camera rolling shutter, so that overall frame rate and speed is only limited by the camera. Furthermore, we note that our scientific camera can acquire faster frames in lower bit modes (8 bit instead of 16 bit), for which, however, no rolling shutter readout mode can be currently utilized, and therefore cannot be used for axial sweeping. In such cases the volume rate can be readily increased to ~ 6 Hz which is the upper limit for our camera and chosen FOV ($1.0 \times 0.7 \times 0.4$ mm, see [Visualization 2](#)). To make use of faster lower bit modes together with axial sweeping, our approach could be combined with galvo-based image-space shearing with the image sensor cropped to the illumination depth of focus [27]. Then a tiling axial sweeping scheme could be used for ETL limited acquisition speeds. The placement of the ETL before the cylindrical lens causes the width and intensity of the light sheet to vary around 5% as it is scanned. This could be avoided by placing it between L_5 and I.

MASOPM joins a growing number of OPM systems designed for larger FOV imaging applications. A major design feature of OPM is the open top geometry, and the ability to use conventional sample mounting such as glass bottomed dishes. We note that using axial sweeping with our design requires the use of #1.0 coverslips – with thicker coverslips the sweep range is limited by optical aberrations (see Fig. S2). The NODO design removes the need for custom optical parts used in a light-sheet mirroring system [12] or blazed OPM [11]. Incorporating axial sweeping gives superior axial resolution over these systems, which are given as $9.2 \mu\text{m}$ and $13.2 \mu\text{m}$, respectively, which would be insufficient for bio-imaging experiments requiring sub-cellular and isotropic resolution. The axial FOV of our implementation is limited by the sensor size and our choice of oblique angle. This could be improved with steeper oblique illumination angles, larger sensors, or scanning on the third microscope. Ultimately the technique would be limited by the lack of higher order corrections of the ETL for focal scanning, which would require remote refocusing.

In conclusion, we have introduced MASOPM as a mesoscopic imaging system with a large volumetric FOV and near-isotropic resolution. The combination of NODO design with axial sweeping enables rapid light-sheet imaging without steric hinderance and axial resolution decoupled from the FOV. Such a system is poised to address complex questions at the intersection of development, neuroscience, and behavior, domains that have historically proven difficult to integrate due to technological constraints. MASOPM will enable the concurrent observation of developmental processes, neural activity, and behavioral dynamics in vivo. This integrated approach is anticipated to yield significant insights into the emergence of organismal complexity.

Funding. International Partnerships for Excellent Education, Research and Innovation (INPART) (Nano-SymBioSys); Fripro Young grant (314546); HORIZON EUROPE Marie Skłodowska-Curie Actions (945405); HORIZON EUROPE Framework Programme (101094250/IMAGINE).

Acknowledgements. We would like to acknowledge support by the EMBL Heidelberg mechanical and electronic workshops, as well as Rory Power, Kaushikaram Subramanian, Rajwinder Singh and Petrus Steenbergen for advice, help and support. We further thank Lars Hufnagel and Suricube GmbH for custom help with the hardware control used in this work.

Disclosures. A.G. is scientific co-founder and advisor of the EMBL spin-off company Suricube GmbH, that makes high performance instrumentation electronics and software commercially available. S.H. is working part-time for Suricube GmbH as an engineer.

Data availability. Data underlying the results presented in this paper is accessible at [28].

Supplemental document. See [Supplement 1](#) for supporting content.

References

1. J. Huiskens, J. Swoger, F. Del Bene, *et al.*, "Optical sectioning deep inside live embryos by selective plane illumination microscopy," *Science* **305**(5686), 1007–1009 (2004).
2. C. Dunsby, "Optically sectioned imaging by oblique plane microscopy," *Opt. Express* **16**(25), 20306 (2008).
3. M. B. Bouchard, V. Voleti, C. S. Mendes, *et al.*, "Swept confocally-aligned planar excitation (SCAPE) microscopy for high-speed volumetric imaging of behaving organisms," *Nat. Photonics* **9**(2), 113–119 (2015).
4. V. Voleti, K. B. Patel, W. Li, *et al.*, "Real-time volumetric microscopy of in vivo dynamics and large-scale samples with SCAPE 2.0," *Nat. Methods* **16**(10), 1054–1062 (2019).
5. B. Yang, M. Lange, A. Millett-Sikking, *et al.*, "DaXi—high-resolution, large imaging volume and multi-view single-objective light-sheet microscopy," *Nat. Methods* **19**(4), 461–469 (2022).
6. M. Kumar, S. Kishore, D. L. McLean, *et al.*, "Crossbill: an open access single objective light-sheet microscopy platform," *bioRxiv*, (2021).
7. E. Sapoznik, B. J. Chang, J. Huh, *et al.*, "A versatile oblique plane microscope for large-scale and high-resolution imaging of subcellular dynamics," *eLife* **9**, e57681 (2020).
8. B. Yang, X. Chen, Y. Wang, *et al.*, "Epi-illumination SPIM for volumetric imaging with high spatial-temporal resolution," *Nat. Methods* **16**(6), 501–504 (2019).
9. E. J. Botcherby, R. Juskaitis, M. J. Booth, *et al.*, "Aberration-free optical refocusing in high numerical aperture microscopy," *Opt. Lett.* **32**(14), 2007–2009 (2007).
10. M. Hoffmann and B. Judkewitz, "Diffractive oblique plane microscopy," *Optica* **6**(9), 1166–1170 (2019).
11. M. Hoffmann, J. Henninger, J. Veith, *et al.*, "Blazed oblique plane microscopy reveals scale-invariant inference of brain-wide population activity," *Nat. Commun.* **14**(1), 8019 (2023).
12. S. Daetwyler, B.-J. Chang, B. Chen, *et al.*, "Mesoscopic oblique plane microscopy via light-sheet mirroring," *Optica* **10**(11), 1571–1581 (2023).
13. W. Shao, M. Chang, K. Emmerich, *et al.*, "Mesoscopic oblique plane microscopy with a diffractive light-sheet for large-scale 4D cellular resolution imaging," *Optica* **9**(12), 1374–1385 (2022).
14. R. Singh, K. Subramanian, R. M. Power, *et al.*, "Oblique plane microscope for mesoscopic imaging of freely moving organisms with cellular resolution," *Opt. Express* **31**(2), 2292–2301 (2023).
15. A. K. Glaser, K. W. Bishop, L. A. Barner, *et al.*, "A hybrid open-top light-sheet microscope for versatile multi-scale imaging of cleared tissues," *Nat. Methods* **19**(5), 613–619 (2022).
16. T. Chakraborty, M. K. Driscoll, E. Jeffery, *et al.*, "Light-sheet microscopy of cleared tissues with isotropic, subcellular resolution," *Nat. Methods* **16**(11), 1109–1113 (2019).
17. K. M. Dean, P. Roudot, E. S. Welf, *et al.*, "Deconvolution-free subcellular imaging with axially swept light sheet microscopy," *Biophys. J.* **108**(12), 2807–2815 (2015).
18. B. Kim, M. Na, S. Park, *et al.*, "Open-top axially swept light-sheet microscopy," *Biomed. Opt. Express* **12**(4), 2328–2338 (2021).
19. S. Park, M. Na, S. Chang, *et al.*, "High-resolution open-top axially swept light sheet microscopy," *BMC Biol.* **21**(1), 248 (2023).
20. K. M. Dean, T. Chakraborty, S. Daetwyler, *et al.*, "Isotropic imaging across spatial scales with axially swept light-sheet microscopy," *Nat Protoc* **17**(9), 2025–2053 (2022).
21. K. W. Bishop, L. A. Erion Barner, E. Baraznenok, *et al.*, "Axially swept open-top light-sheet microscopy for densely labeled clinical specimens," *Opt. Lett.* **49**(13), 3794 (2024).
22. M. Kumar, S. Kishore, J. Nasenbeny, *et al.*, "Integrated one- and two-photon scanned oblique plane illumination (SOPi) microscopy for rapid volumetric imaging," *Opt. Express* **26**(10), 13027 (2018).
23. A. Stokkermans, A. Chakrabarti, K. Subramanian, *et al.*, "Muscular hydraulics drive larva-polyp morphogenesis," *Curr. Biol.* **32**(21), 4707–4718.e8 (2022).
24. N. Banterle, K. H. Bui, E. A. Lemke, *et al.*, "Fourier ring correlation as a resolution criterion for super-resolution microscopy," *J. Struct. Biol.* **183**(3), 363–367 (2013).
25. X. Luo, Z. Zhou, J. Huang, *et al.*, "Resolution evaluation method and applications of 3D microscopic images," *Zhongguo Jiguang/Chinese Journal of Lasers* **49**(5), 0507205 (2022).
26. A. Paix, S. Basu, P. Steenbergen, *et al.*, "Endogenous tagging of multiple cellular components in the sea anemone *Nematostella vectensis*," *Proc. Natl. Acad. Sci. U. S. A.* **120**(1), e2215958120 (2023).
27. B. J. Chang, J. D. Manton, E. Sapoznik, *et al.*, "Real-time multi-angle projection imaging of biological dynamics," *Nat. Methods* **18**(7), 829–834 (2021).
28. S. Davis, J. R. Sommers, S. Hambura, *et al.*, "Mesoscopic axially swept oblique plane microscope for imaging of freely moving organisms with near-isotropic resolution," Zenodo, 2024, <https://doi.org/10.5281/zenodo.13829926>.